Journal of Alloys and Compounds 775 (2019) 304–315

Contents lists available at ScienceDirect

Journal of Alloys and Compounds

journal homepage: http://www.elsevier.com/locate/jalcom

Structural, morphological, Raman and ac electrical properties of the multiferroic sol-gel made $Bi_{0.8}Er_{0.1}Ba_{0.1}Fe_{0.96}Cr_{0.02}Co_{0.02}O_3$ material

A. Benali [a, b, *], B.M.G. Melo [a], P.R. Prezas [a], M. Bejar [b], E. Dhahri [b], M.A. Valente [a], M.P.F. Graça [a], B.A. Nogueira [c], B.F.O. Costa [d]

[a] I3N, Physics Department, University of Aveiro, Campus de Santiago, Aveiro, Portugal
[b] Laboratoire de Physique Appliquée, Faculté des Sciences, Université de Sfax, B.P. 1171, 3000, Sfax, Tunisia
[c] CQC, Department of Chemistry, University of Coimbra, P-3004-535, Coimbra, Portugal
[d] CFisUC, Physics Department, University of Coimbra, Rua Larga, P-3004-516, Coimbra, Portugal

ARTICLE INFO

Article history:
Received 23 August 2018
Received in revised form
11 October 2018
Accepted 12 October 2018
Available online 13 October 2018

Keywords:
Multiferroic
Ceramics
Impedance spectroscopy
Bismuth ferrite
Perovskite

ABSTRACT

We have investigated the effect of multi-doping in A and B site of the multiferroic prepared by the Sol-gel method $Bi_{0.8}Er_{0.1}Ba_{0.1}Fe_{0.96}Co_{0.02}Cr_{0.02}O_3$ (**BEBFCC**) on the structural, morphological and electric properties. X-Ray diffraction and Rietveld refinement confirm that the BEBFCC compound presents a rhombohedral structure with the *R3C* space group. The *Ac* electrical properties have been measured from 331 to 735 K as a function of frequency (100 kHz - 1 MHz). Debye's theory and Arrhenius relations were used to study the relaxation phenomenon. The frequency dependence of the impedance (Z": imaginary part) reveals the existence of one relaxation peak, while the Modulus formalism shows two peaks. The presence of two contributions, related to the dielectric relaxations visible in this compound, was confirmed by the Impedance Nyquist plots. The study of the ac conductivity based on Jonsher's power law confirms that the conduction is associated to the Non-Overlapping Small Polaron Tunneling model.

1. Introduction

Materials that exhibit simultaneous order in their electric and magnetic ground states hold promising application in next-generation memory devices in which the electric field can control the magnetic state. Due to the different structural requirements necessary for the same material having ferroelectricity and magnetism responses makes such materials rare. Despite the recent identification of several new multiferroic materials and also magnetoelectric coupling mechanisms [1–4], the amount of known single-phase multiferroic materials is still limited by antiferromagnetic or weak ferromagnetic alignments. This is mainly due to the lack of coupling between the ferroelectric and magnetic order parameters [5] or by having properties that emerge only well below room temperature [6,7], precluding device's applications [8].

Among the different types of multiferroic compounds, bismuth ferrite ($BiFeO_3$; BFO) stands out because it is perhaps the only one being simultaneously magnetic and strongly ferroelectric at room temperature [9,10]. The ability to control the magnetic and ferroelectric properties of multiferroic $BiFeO_3$ (BFO) by cationic substitution into Bi- and Fe-sites using rare earth (RE) and transition metal (TM) ions opens up promising opportunities for designing new multiferroic materials [11,12].

Obviously, the small magnetization, weak polarization and the low electrical resistivity are the critical drawbacks of BiFeO3 materials that hinder its broad industrial application. As mentioned, the substitution in A and B sites by rare-earth ions [13–15] and by transition metal ions [16–19], respectively enhance simultaneously ferroelectric and ferromagnetic properties. It has been argued that the 10% substitution of Bi ions by Er^{3+} ones enhance only the ferroelectric property [20]. Also for the same sample, partial substitution of bismuth ions by barium ones enhance the magnetic property [21]. On the other hand, it was reported that double substitution of iron ions by 2% of Mn and/or 2% of Co ones showed a good magnetic and ferroelectric behaviors [22,23]. To our knowledge, there is no report on the simultaneous substitution of Er and Ba ions on the A-site of $BiFeO_3$ matrix with B-site simultaneous substitution with Cr and Co ions.

Taking the previous results into account, in this work we discuss the structural, morphological and dielectric properties of a BFO

* Corresponding author. I3N, Physics Department, University of Aveiro, Campus de Santiago, Aveiro, Portugal.
E-mail address: benaliadel96@gmail.com (A. Benali).

https://doi.org/10.1016/j.jallcom.2018.10.142
0925-8388/

system with a 20% of Er^{3+} and Ba^{2+} (10% for each one) and 4% of Co^{2+} and Cr^{3+} (2% each one) substitution of Bi^{3+} and Fe^{3+} ions, respectively.

2. Experimental methods

The nanocrystalline $Bi_{0.8}Er_{0.1}Ba_{0.1}Fe_{0.96}Cr_{0.02}Co_{0.02}O_3$ (**BEBFCC**) powder was prepared by the sol-gel method [24,25]. The raw materials used for the precursor solutions were Bismuth nitrate, Erbium nitrate, Barium nitrate, ferric nitrate, Chromium nitrate, Cobalt (II) nitrate and citrate acid (purity ≥ 99%, from Sigma Aldrich). The first step consisted of dissolving separately all nitrates in ion-free water at room temperature. Bismuth nitrate (5 mol% excess) was added to the mixed solution to compensate the Bi evaporation. Then, citrate acid (metal complex agent) and ethylene glycol were added to the solution mixture which has been stirred at 70 °C for 3 h until obtaining a viscous gel. After this, the gel was dried at 170 °C, and the obtained powder was carefully crushed to form a fine powder. The dried powder was calcinated at 300 °C for 12 h, and afterward gridded again. Pellets of approximately 10 mm in diameter and 1.5 mm in thickness were made using a uniaxial pressure system. The pellets were heat-treated, first, at 600 °C for 12 h, and then at 800 °C for 4 h.

The phase and structure of the as-prepared powder were determined by X-Ray Diffraction (XRD) using a Bruker 8D Advance X-ray powder diffractometer, with $CuK_{\alpha 1}$ radiation ($\lambda = 1.5406$ Å). The XRD data was also used for obtaining the lattice parameters applying Rietveld's analysis [26], using the FullProf software.

Room temperature (RT) Raman spectroscopy was performed under backscattering geometry, using a Jobin Yvon HR 800 system and an excitation wavelength of 473 nm. The Raman spectra were recorded with a modular double-grating excitation spectrofluorimeter with a TRIAX 320 emission monochromator (Fluorolog-3, Horiba Scientific) coupled to an HR 980 Hamamatsu photomultiplier, using a front face acquisition mode. As an excitation source, a 450 W X arc lamp was used [27].

The dielectric measurements were performed in air atmosphere using an electric furnace equipped with a Eurotherm 3508 controller. For these measurements a Network Analyzer Agilent 4294, operating between 100 Hz and 1 MHz in the Cp-Rp configuration (capacitance in parallel with resistance) was used [28]. This non inductive electrical furnace operates from room temperature up to 735 K. During the measurement, the sample was mechanically pressed between two parallel platinum plates working as electrodes. The ac impedance of the samples was measured between room temperature and 735 K.

3. Results and discussions

3.1. Structural properties

The X-ray diffraction pattern of the synthesized BEBFCC sample is shown in Fig. 1. All the major peaks in the diffraction patterns could be indexed to various (hkl) planes of $BiFeO_3$ and match perfectly with the rhombohedral structure (R3C space group) of pure $BiFeO_3$ (*JCPDS file no. 71-2494*) [29]. All diffraction peaks were intense and sharp, indicating the highly crystalline nature of the samples. Minor impurity peaks were also evident in the XRD patterns and the indexation and refinement done in X'Pert HighScore showed that they correspond to the $Bi_2Fe_4O_9$ and $Bi_{25}FeO_{40}$ phases. The formation of these secondary phases during the synthesis of bulk undoped BFO and cations substituted BFO was almost unavoidable in some previous investigations [30–33].

The refinements were carried out using the structure of undoped $BiFeO_3$ as a starting model, and using the space group R3C with lattice constants a = 0.5587 nm, b = 0.5587 nm and c = 1.386 nm. There is a good agreement between the experimental and XRD refinement data as one can see in Fig. 1. The variation of the lattice constants of the **BEBFCC** sample is summarized in the table inset of Fig. 1.

The average Crystallite sizes (D_{SC}) were estimated from the XRD patterns, using the Scherrer's formula [34]:

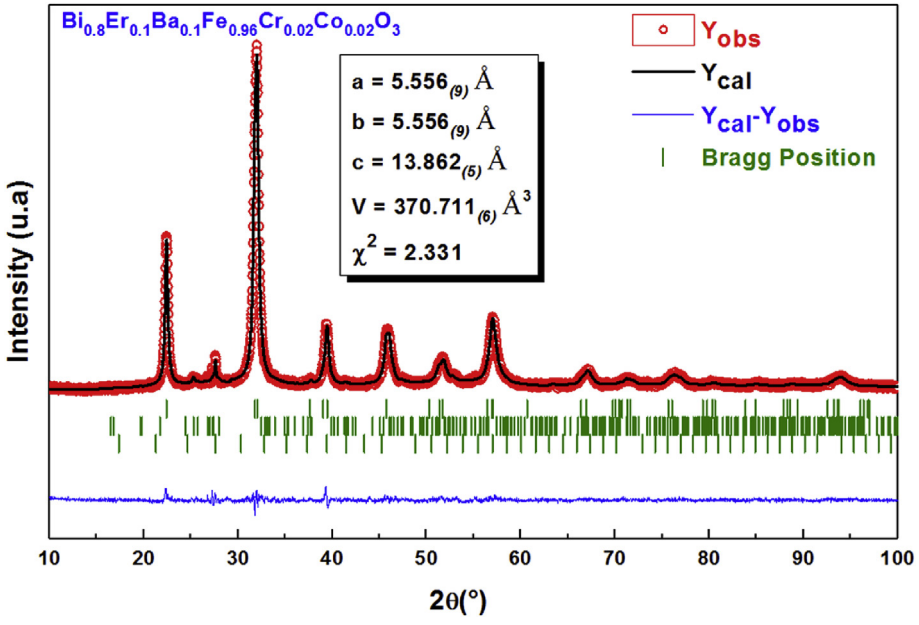

Fig. 1. Refined X-ray diffraction patterns of Sol–Gel driven BBEFCCO compound: Solid black circle represents the observed pattern; continuous red line represents calculated pattern and the blue line represents difference between the observed and calculated patterns. Tick green markers correspond to the position of the allowed Bragg diffractions. (For interpretation of the references to colour in this figure legend, the reader is referred to the Web version of this article.)

$$D_{sc} = \frac{0.9 \times \lambda}{\beta \times \cos\theta} \quad (1)$$

where λ is the applied wavelength, θ is the Bragg angle for the most intense peak, and β is the half height width of this peak. The average crystallite size was found to be around 68 nm.

3.2. Morphological study

The surface morphology of these materials was studied by Scanning Electron Microscopy (SEM). Fig. 2 (a) depicts the room temperature SEM micrographs of the Multiferroic $Bi_{0.8}Ba_{0.1}Er_{0.1}Fe_{0.96}Co_{0.02}Cr_{0.02}O_3$ compound. From this spectrum, one can see that the grains have an irregular morphology (spherical, cube, polygonal…) and that they are non-uniformly distributed which are similar to those of the pure BFO compound (inset of Fig. 2 (a)) [35]. A manual statistical count of the grain size was performed on SEM images using the Image J software. The results are expressed in Fig. 2(b) as grain number (counts) vs. particle size (nm). These particles were distributed, for the BBEFCC sample, according to a Lorentzian distribution (Red solid line in Fig. 2 (b)). The average particle size, generally known as grain, was found to be 88 ± 2 nm, which is greater than that of the average crystallite size determined by XRD (68 nm). This can be explained by the fact that each particle observed by SEM is formed by several crystallized grains.

The composition and purity of the prepared compound were confirmed by energy dispersive X-ray microanalysis (EDX), and X-ray fluorescence (XRF) experiments. Illustrative results are presented in Fig. 2(c) and (d) and summarized in Table 1. The EDX spectra show characteristic features of all expected elements (Bi, Ba, Er, Fe, Cr and Co), which confirms that there was no loss of any integrated element during synthesis. The same result was confirmed by the XRF data.

Table 1
XRF results of the BBEFCCO compound.

Z	Elem	Elem Name	Line	A cps	ROI keV
24	**Cr**	Chromium	Ka	270.327	5.25–5.58
26	**Fe**	Iron	Ka	10015.997	6.23–6.57
27	**Co**	Cobalt	Ka	3713.842	6.75–7.10
56	**Ba**	Barium	Ka	882.520	31.75–32.37
68	**Er**	Erbium	La	3868.023	6.77–7.12
83	**Bi**	Bismuth	La	79343.500	10.62–11.03

3.3. Raman spectroscopy

In BFO 18 optical phonon modes are expected. These can be summarized using the irreducible representation: $\Gamma_{opt} = 4A_1 + 5A_2 + 9E$. According to the group theory, 13 of these modes are Raman active ($\Gamma_{Raman,R3c} = 4A_1 + 9E$), whereas the remaining (the 5A2 modes) are not active using Raman spectroscopy [36,37]. Hermet et al. [38] suggested that Bi atoms mainly participate in the low-frequency modes (up to 167 cm^{-1}, i.e., the modes E, $A_{1\text{-}1}$, and $A_{1\text{-}2}$) and that the motion of oxygen atoms dominates the high-frequency modes, namely the modes above 262 cm^{-1}, while Fe atoms participate in the modes between 152 and 262 cm^{-1} with possibility of affecting higher frequency modes. Moreover, it is also known that the Bi–O bonds are associated with the low-frequency modes (below 170 cm^{-1}) and the intermediate frequency modes (above 270 cm^{-1}), respectively [39]. The vibrational mode near 221 cm^{-1} is the A_{1-3} tilt mode of the FeO_6 octahedron, and some higher frequency modes (around 670 cm^{-1}) are also involved in the Fe–O bonds [40].

Fig. 3 (a) shows the Raman spectrum of pure BFO and the

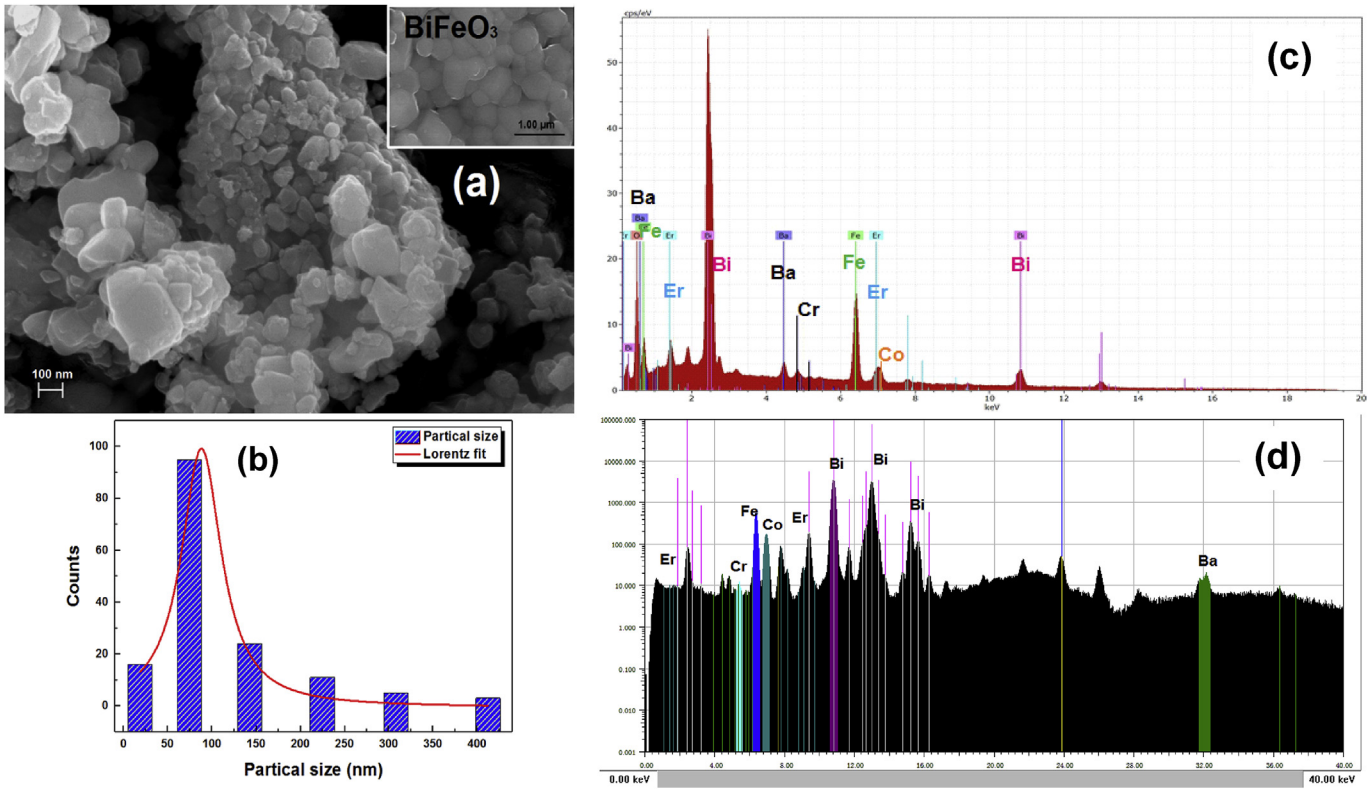

Fig. 2. **(a)** SEM image of surface morphologies, **(b)** particle size distributions, **(c)** EDX and XRF **(d)** Spectra of the **BBEFCCO** compound.

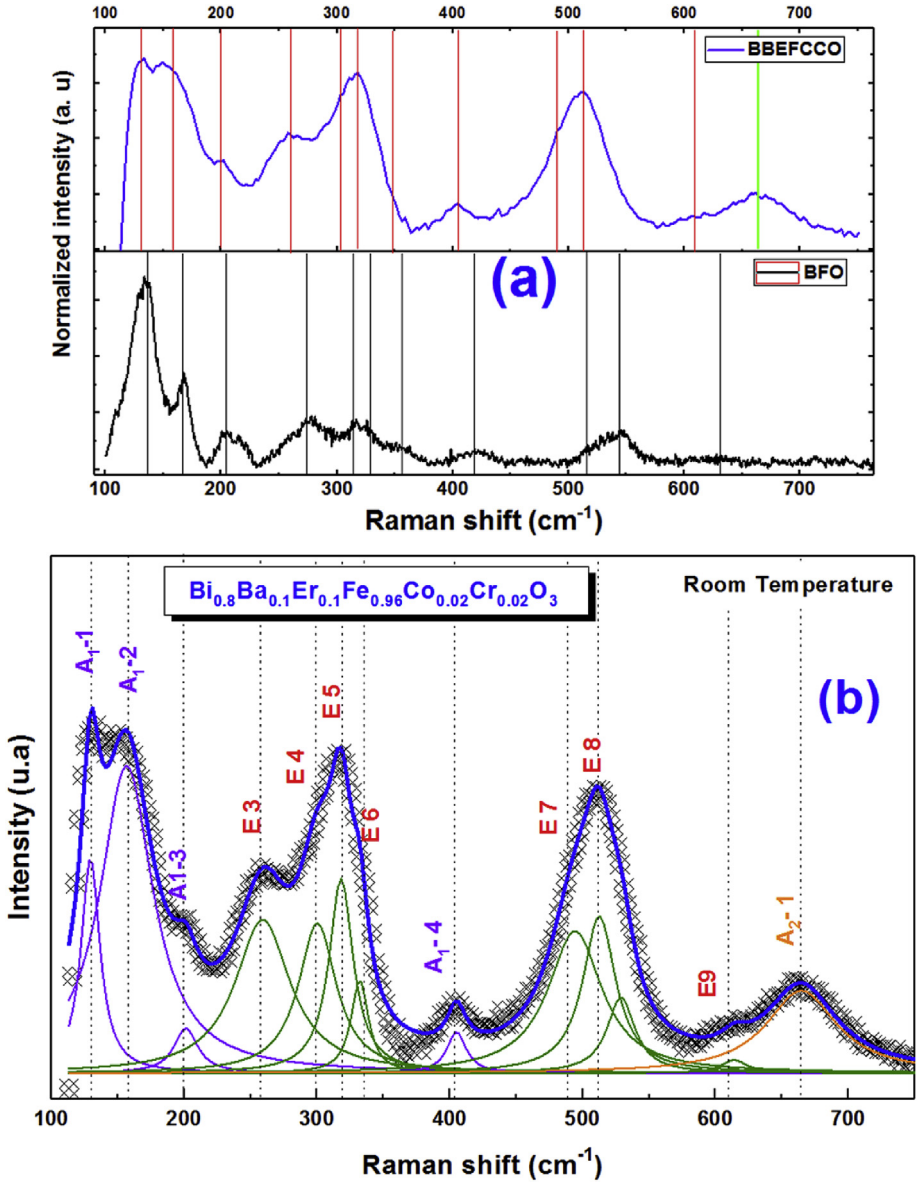

Fig. 3. **(a)** Room temperature Raman spectrum of pure BFO and BEBFCC compounds, **(b)** Deconvoluted first order Raman modes for the BBEFCC compound.

studied BEBFCC compounds which reveals the presence of almost of the Raman active modes of the pure BFO with 7 peaks correspond to the E (TO) modes and 4 A1 modes [35]. Which confirms the rhombohedral perovskite structure of the prepared **BEBFCC** compound.

As it is evident in Fig. 3 (b) and summarized in Table 2, the Raman vibrational modes of the present **BEBFCC** studied sample slightly shifts to lower frequency with the enhance intensity of E modes, specially the E9 and E5 modes. The intensity enhancement of the E9 mode at around 611 cm^{-1} could be related mainly to the variation in Fe–O bonds due to the to the distortion of the (Fe/Cr/Co)O_6 octahedra. Also, the close merge of the A_{1-1} and A_{1-2} modes, comparing to BFO Raman spectra, indicates a stretch of Bi–O bonds due to the insertion of Er and Ba ions.

3.4. Impedance spectroscopy

Fig. 4 (a) shows the frequency dependence of the imaginary part of impedance (Z″) at different temperatures. The Z″ spectra is characterized by the appearance of a peak for each temperature at a specific frequency suggesting the existence of a dielectric relaxation in the BEBFCC compound. It is also noted that all Z″ peaks were

Table 2
Observed Raman modes for pure BFFO and BEBFCC compounds.

Sample	A_{1-1}	A_{1-2}	A_{1-3}	E-3	E-4	E-5	E-6	A_{1-4}	E-7	E-8	E-9	A_{2-1}
BFO [35]	134	166	216	273	315	327	356	419	515	545	631	–
BEBFCC	138	165	230	254	276	305	349	463	486	526	614	664

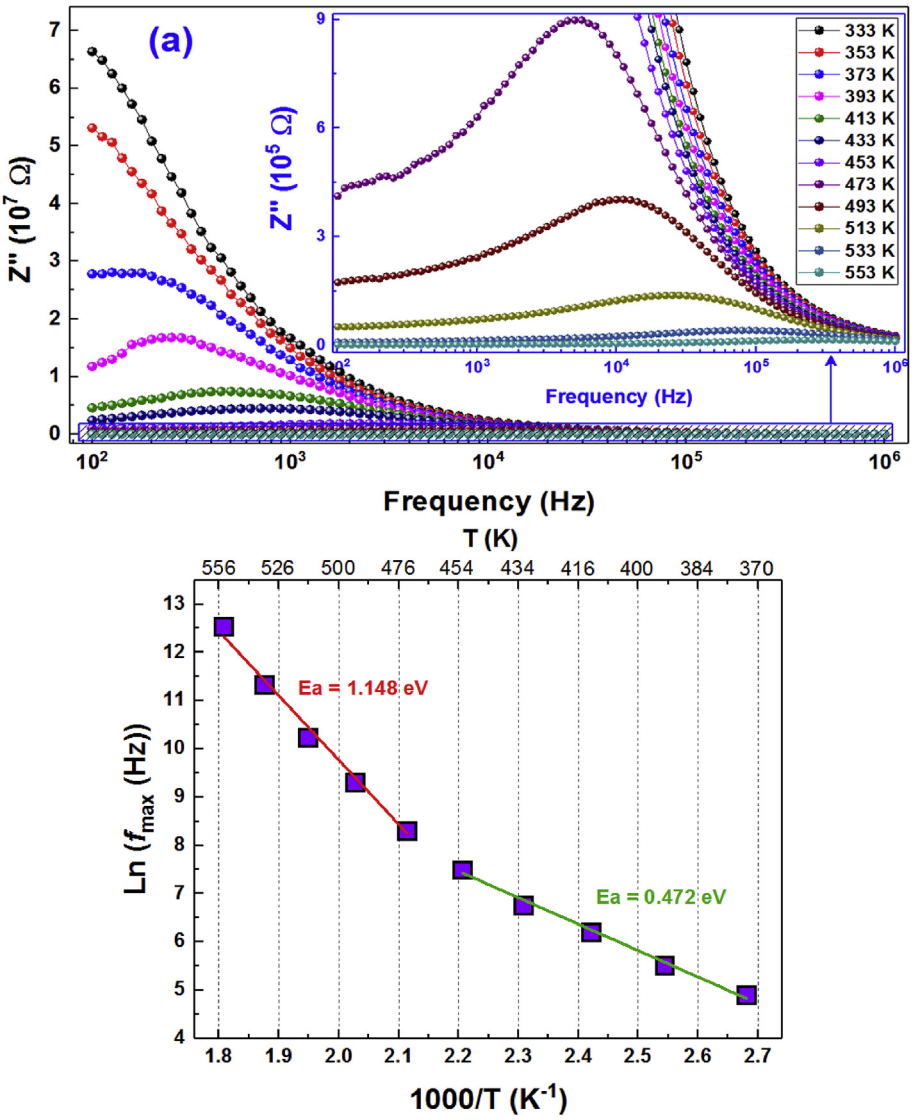

Fig. 4. **(a)** The frequency dependence of the imaginary part of the complex electrical impedance (Z″) at several measurement temperatures of the BBEFCC compound **(b)** the Arrhenius plots shows dependence f_{max} (peak of Z″) vs. 1/T.

found to shift towards higher frequency with the increase in temperature. These observations are supportive of the previous results to confirm the semiconducting behavior of the suggested sample and to prove the implication of charge carriers in the relaxation phenomena and their thermal activation [41].

On the other hand, for all peaks, the decrease of the values Z''_{max} values with the increase of temperature could be explained by the reduction of the resistance of materials [42]. Furthermore, the coalescing of all these curves at higher frequencies (over 10^5 Hz) mimics the reduction of space charge polarization with the increase in frequency [43].

The activation energy of the dielectric relaxation process was determined using the Arrhenius law. The variation of relaxation frequency (f_{max}) with temperature can be expressed by Eq. (2) [44]:

$$f_{max} = f_0 \exp\left(-\frac{E_a}{k_B T}\right) \quad (2)$$

where f_0 is the relaxation frequency for high temperature, E_a the activation energy for the relaxation process and k_B the Boltzmann constant.

The logarithmic representation of the deduced f_{max} values is plotted as function of the inverse of temperature in Fig. 4 (b) using the Arrhenius model. It is clear from the figure the existence of two remarkable regions were the activation energy change from a region to the other. The obtained values of activation energy are 0.472 and 1.148 eV below and above 453 K, respectively. These values are in good agreement with the result obtained in the literature [45,46].

Moreover, the Impedance Nyquist plot (-Z″ versus Z′) of the **BEBFCC** compound at different temperatures are presented in Fig. 5. These plots are characterized by two semicircular arcs that are not centered on the real axis. The decentralization is indicative of non-Debye type relaxation process, and the material was found to obey the to the Cole-Cole formalism [47–49]. Each semicircle can be attributed to a given contribution. Namely, at low frequencies, the semicircle can be attributed to the grain boundary contribution, and at high frequency, the semicircle is attributed to grain contribution. The red lines in Fig. 5 show the simulated Nyquist plots with the equivalent circuit elements, at several temperatures. This

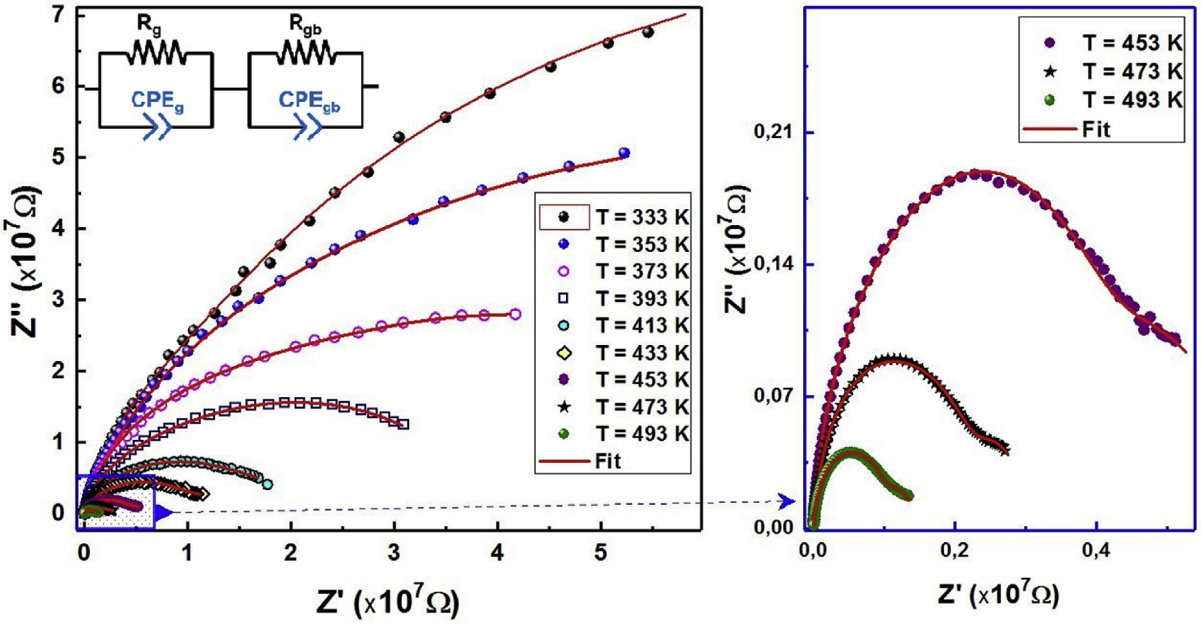

Fig. 5. The fit of the experimental data using Z-view software. The inset shows the equivalent circuit formed by two parallel combination of resistance and constant phase element impedance (R-CPE circuit).

circuit is modeled by a combination series of two parallel R-CPE circuits, with R representing the resistance and CPE the constant phase element (capacity of the fractal interface). The variables R_1, CPE_1 and R_2, CPE_2 represent the resistance and capacitance of grains and grain boundaries, respectively. The CPE impedance (Z_{CPE}) is given by the following relation [50,51]:

$$Z_{CPE} = \left[Q(j\omega)^{\alpha}\right]^{-1} \tag{3}$$

where Q is a proportional factor, ω is the angular frequency, and α is an empirical exponent close to 1. Depending on the value of the exponent α, the CPE has a behavior similar to the components conventionally used in equivalent circuits. The CPE is reduced to a resistance and ideal capacitive elements when it is close to Zero and $\alpha = 1$, respectively. The calculated R, CPE and α parameters are summarized in Table 3. It is clear that the resistance values decrease with the increase of temperature, which can be explained by the increased mobility of the charge carriers that contribute to the conduction process [52].

The resistance at these temperature values can be deduced from the well-defined impedance peak, which was found to follow the Arrhenius relation:

Table 3
Values of electrical parameters deduced from the complex diagram at several temperatures for BBEFCCO compound.

T(K)	R_1 ($10^6\,\Omega$)	C_1 (10^{-11} F)	α_1	R_2 ($10^6\,\Omega$)	C_2 (10^{-11} F)	α_2
333	**483.1**	1.373	0.988	**82.65**	5.493	0.964
353	**200.1**	1.921	0.969	**13.06**	8.508	0.966
373	**79.45**	2.380	0.954	**6.722**	9.093	0.922
393	**31.07**	3.489	0.934	**2.666**	21.27	0.932
413	**12.21**	4.012	0.923	**1.053**	35.21	0.941
433	**7.51**	5.899	0.898	**0.825**	31.40	0.917
453	**3.33**	4.542	0.902	**0.394**	55.23	0.939
473	**1.51**	5.780	0.867	**0.133**	61.32	0.931
493	**0.89**	6.003	0.855	**0.0789**	77.03	0.980

The activation energy of grains and boundary grains will be calculated using the resistance values mentioned in bold in Table 3.

$$R = R_0 \exp\left(\frac{E_{ac}}{k_B T}\right) \tag{4}$$

where R_0 is the per-exponential term, and E_{ac} is the activation energy. The linear fitting based on Eq. (4) shown in Fig. 6 as a straight line yields the values of $E_{ac} = 0.517$ and 0.530 eV for R_g and R_{gb}, respectively. It was confirmed that a p-type polaronic hopping conduction is observed with activation energy higher than 0.2 eV [53]. The activation energy associated to grains and boundary grains are found to be around 0.5 eV which shows the presence of p-type polaron hopping conduction mechanism. In the other hand, similar values of activation energy was attributed to the oxidation of Fe^{3+} ions to Fe^{4+} ones [54].

Fig. 7 shows the frequency and temperature dependence of the imaginary part of the dielectric modulus. This 3D graphic indicates very clearly the presence of two dielectric relaxations, one visible at

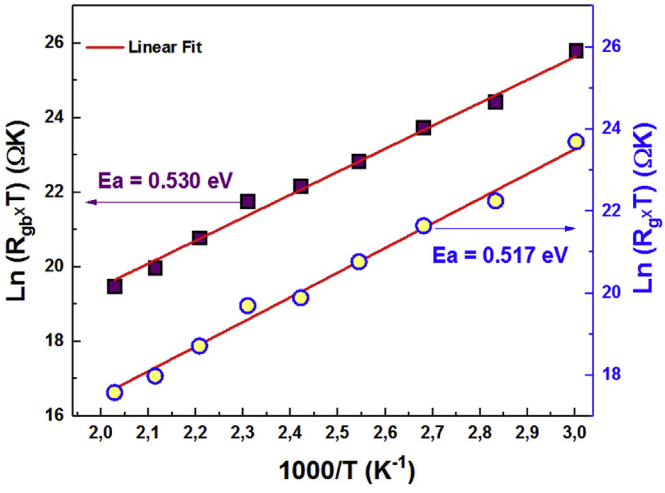

Fig. 6. The Arrhenius plots for BEBFCC compound logarithm of resistances vs. 1/T.

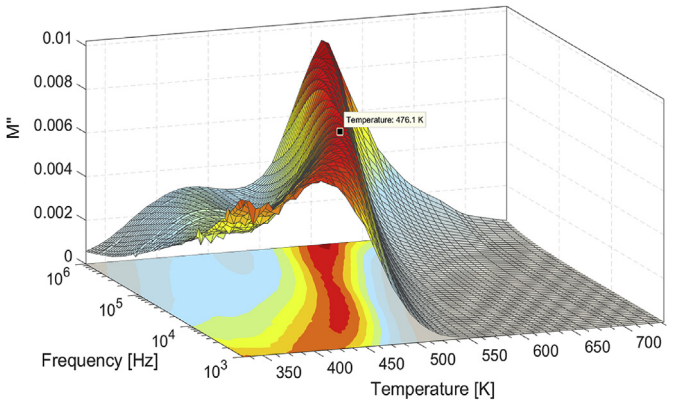

Fig. 7. 3D graphic of the M″ dependence on frequency and temperature.

lower temperatures and centered at higher frequencies and a second relaxation which is visible at higher temperatures. While the first relaxation cannot be examined because it shifts to frequencies out of the examined window, the latter relaxation can be studied over a wide range of temperatures and reveals the evolution of a thermally activated relaxation peak that shifts towards higher frequencies with increasing temperature. Moreover, at around 476 K this relaxation peak shows an inflection point, suggesting a different (faster) response of the electric dipoles at higher temperatures.

To further investigate the dielectric relaxation seen in Fig. 7, the frequency dependence of M″ was plotted in Fig. 8 (a). As previously discussed, at lower temperatures the spectrum shows the appearance of two dielectric relaxations, one at low and another at high frequencies. However, above 414 K the secondary relaxation centered at higher frequencies shifts out of the examined frequency

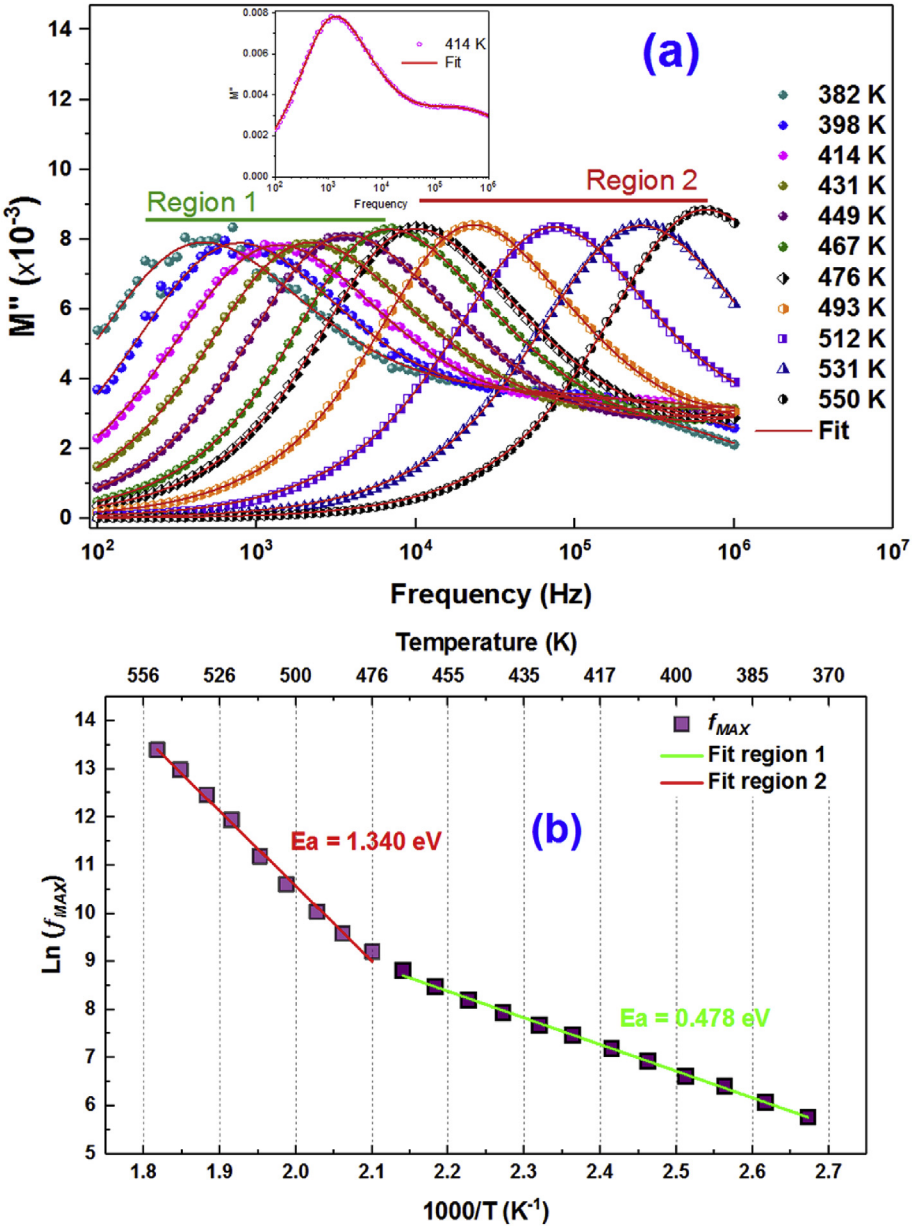

Fig. 8. **(a)** The frequency dependence of the imaginary part of the complex electrical Modulus (M″) at several measurement temperatures (plot at 414 K in the graphic inset) of the BBEFCC compound **(b)** Arrhenius plots showing the f_{max} (peak of M″) dependence vs. 1000/T.

range. Therefore, the relaxation discussed in this work will be the one visible up to 550 K. The relaxation spectra of the sample were adjusted to the empirical Havriliak-Negami (HN) relaxation function using the software *Winfit*. As one can see, there is a good agreement between the experimental data and the fitted function. Based on the HN fitting, the frequency of the relaxation's peak maximum (f_{MAX}) was determined. The activation energy of the relaxation was calculated based on Eq. (2) and on the frequency of the peak maximum. Fig. 8 (b) presents the natural logarithmic variation of f_{MAX} vs. 1000/T. As one can see, from 374 K to 550 K there are two distinct regions with different activation energies (also labeled in Fig. 8 (a)). From 374 K to 467 K the activation energy of the dielectric relaxation is around 0.478 eV, while above 476 K the activation energy increases significantly (1.34 eV). Fig. 7 revealed an inflection point at this temperature, suggesting that in fact there is a variation in electric dipoles response. The greater activation energy for temperatures above 476 K could be related with either a phase transition or due to the contribution of a new type of electric dipoles that are activated at 476 K [55,56]. One possible explanation would be that the newly polarized dipoles are less mobile and hence the activation energy of the dielectric relaxation increases.

The dielectric constant (ε') and dielectric loss (ε'') values of the BEBFCC compound, plotted at several temperatures, are shown in Fig. 9 (a) and (b). As expected, ε' decreases with frequency and increases as the temperature rises. As for the ε'', one can see that it also increases with temperature, and above 604 K the ε'' values decrease logarithmically with frequency. Another result worth notice is that using the ε'' formalism the dielectric relaxation previously discussed is not visible.

Fig. 9 (c) displays the temperature dependence of the dielectric constant at 1 kHz, 10 kHz, 50 kHz, and 100 kHz. For all frequencies, ε' shortly increases up to 470 K, and afterward, between 470 and 500 K increases sharply with temperature. This behavior is consistent with the variation seen around this temperature in the activation energy of the dielectric relaxation (Fig. 8 (b)). This could mean that either there is a phase transition at this temperature, or that the mobility of the charge carriers increases and allows them to flow to the grain boundaries where they can form electric dipoles.

The Nyquist (M^*) plots of the BEBFCC sample are shown in Fig. 10. Usually, the Modulus formalism is known to magnify the grain effects and to minimize the electrode polarization effect. Hence, oppositely to the Nyquist (Z^*) plot in Fig. 5, when analyzing the Nyquist (M^*) of ceramic materials, two responses (due to grain and grain boundaries) can be identified. Fig. 10 shows one semicircle at higher frequencies related to the grain/bulk contribution, and another one at higher frequencies due to the grain boundaries. As one can see, the grain contribution becomes less prominent as the temperature increases, and at higher temperatures, one can only distinguish the grain boundary semicircle.

3.5. ac conductivity and conduction mechanism

Fig. 11 shows the $\ln(\sigma_{ac} \times T)$ vs. 1000/T dependence for several frequencies. Below 500 K the ac conductivity is low and is not thermally activated. At around 500 K are thermally activated some charge carriers with higher mobility, and the ac conductivity sharply increases. From 493 K up to 578 K, the σ_{ac} activation energy is around 1.303 eV and the conductivity displays a nearly frequency independent behavior. This value is very close to the activation energy calculated in the region 2 of the dielectric relaxation studied, which suggest that the mechanism responsible for the σ_{ac} may be similar to the relaxation mechanism.

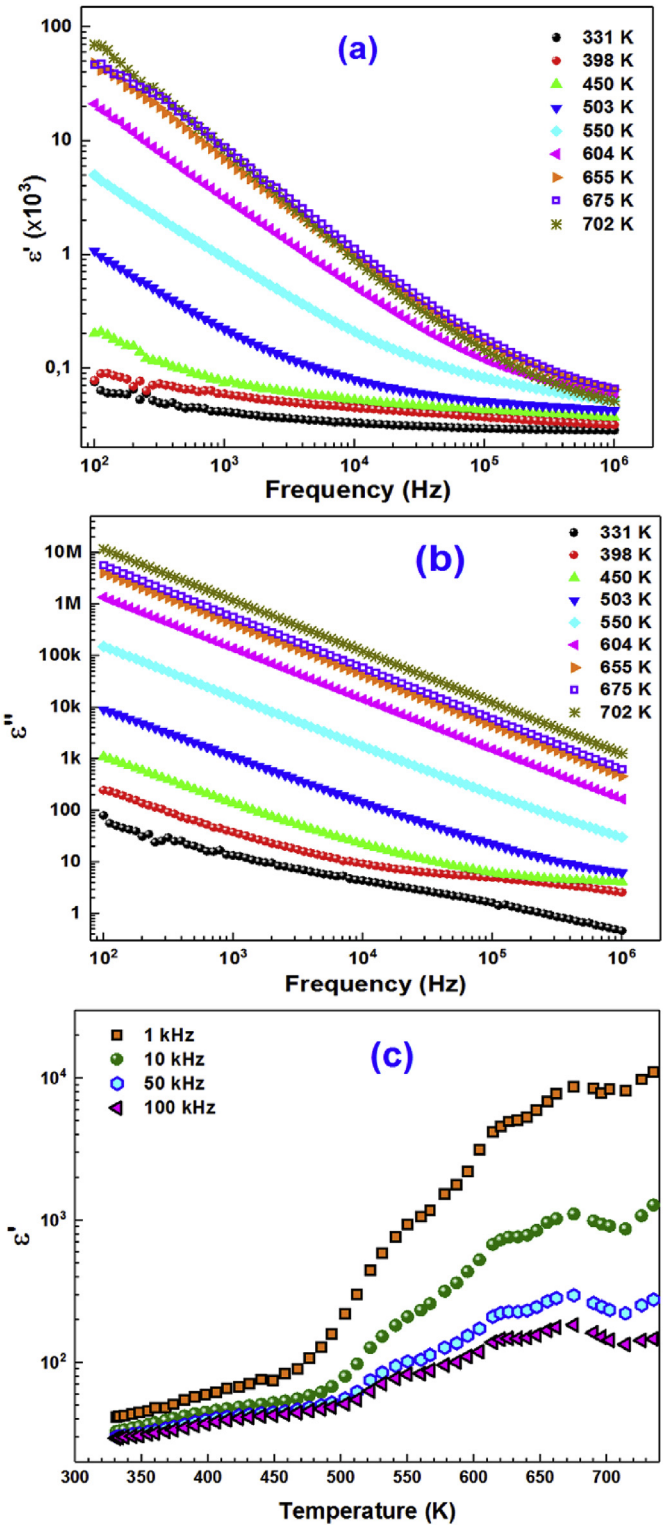

Fig. 9. Frequency dependence of (a) Dielectric constant and (b) dielectric loss values of the BEBFCC compound, (c) Dielectric constant of the BEBFCC compound as a function of temperature.

The graphic inset of Fig. 11 shows that the temperature transition point between the near frequency independent and the frequency dependence region shifts towards higher frequencies with increasing temperature. The latter behavior can be explained by the increased influence of the dc conductivity component, overcoming

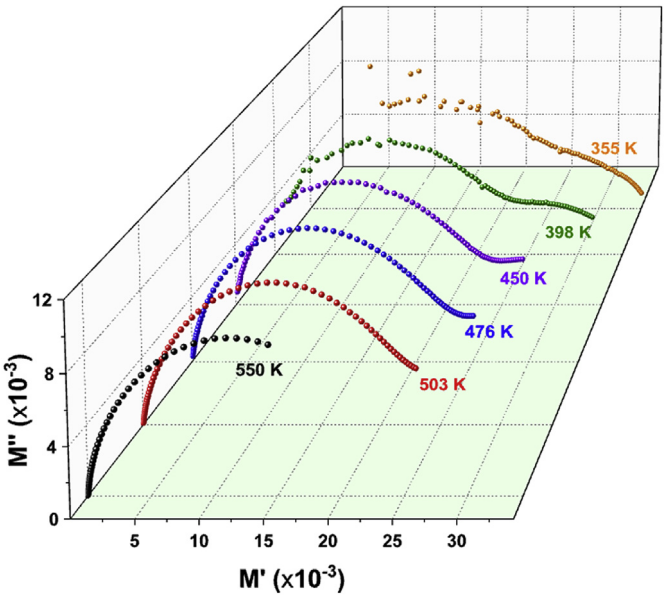

Fig. 10. Nyquist (M*) plot of the dielectric modulus, for the BEBFCC sample.

the ac contribution at temperatures above 604 K. For temperatures above 678 K the ac conductivity follows the Arrhenius model once again, and the activation energy in this temperature range decreases to 0.825 eV.

Since the ac conductivity becomes nearly frequency independent in the examined frequency range above 500 K, the conduction mechanism of the BEBFCC compound will be further discussed only for temperatures below 500 K by analyzing the temperature dependence of the Jonscher's power-law *S* parameter.

Fig. 12 (a) shows the 3-D frequency and temperature dependence of the ac conductivity of the BEBFCC monocrystalline compound. One can notice two different regions in the ac conductivity; the low-frequency region, where the conductivity is unaffected by the frequency and the high-frequency region, where, unlike in the first region, an increase in frequency is followed by an increase in the conductivity values. The origin of the frequency dependence of the conductivity can be due to the relaxation of the ionic atmosphere after the movement of the particle [57].

The frequency dependence of the conductivity generally obeys the Jonscher's power-law [58]:

$$\sigma_{ac} = \sigma_{dc} + A\omega^{S} \quad (5)$$

where σ_{ac} is the alternating current conductivity, σ_{dc} is the direct current conductivity of the sample and ω is the angular frequency of measurement. The exponent **"S"** represents the degree of interaction between mobile ions with the lattices around them, and A is a constant which determines the strength of polarizability. The σ_{dc} at different temperatures can be obtained according to a nonlinear fitting based on Eq. (5) and the adjusted results of the electrical conductivity are summarized in Table 4.

The conduction mechanism in the BEBFCC compound was determined by analyzing the temperature dependence of the parameter "S". As one can see in Fig. 12 (b), this parameter was found to increase with increasing temperature. The appropriate model of the conduction mechanism of the ac conductivity could be suggested from the correlation between the S (T) behavior and the conduction mechanism of the ac conductivity [59].

In the literature, different models have been considered based on two distinct processes, namely, classical hopping over a barrier and quantum-mechanical tunneling, or some variant or combination of the two, and it has been differently assumed that the responsible charge carriers can be either electrons (or polarons) or atoms [60]. These different models are:

The **Q**uantum **M**echanical **T**unneling (QMT) model, the exponent "S" is virtually equal to 0.8 and independent of temperature or increases slightly with temperature [61,62].

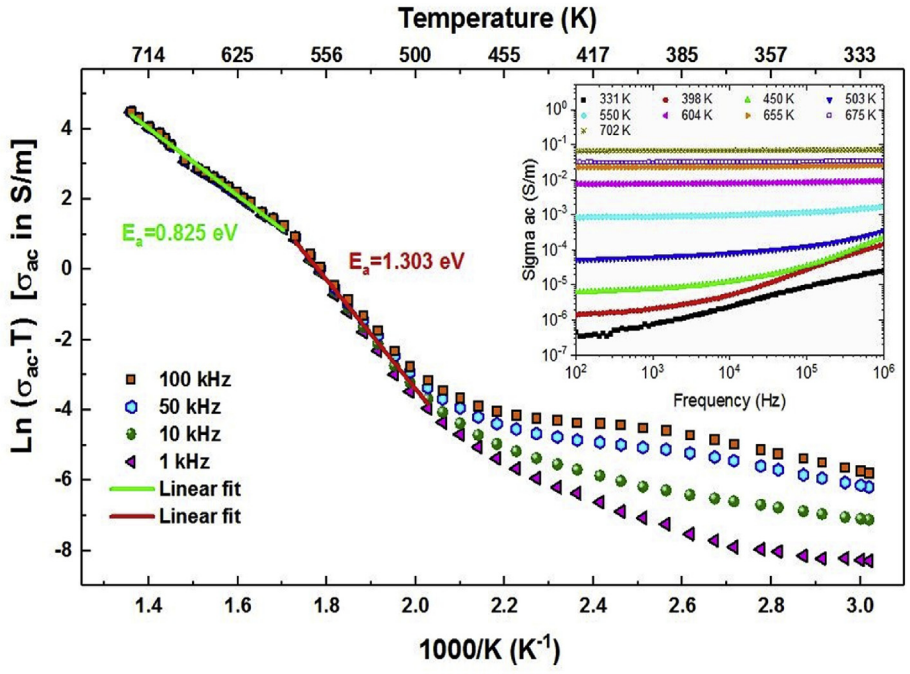

Fig. 11. Linearization of σ_{ac} using the Arrhenius equation. Frequency dependence of σ_{ac} at several temperatures in the graphic inset.

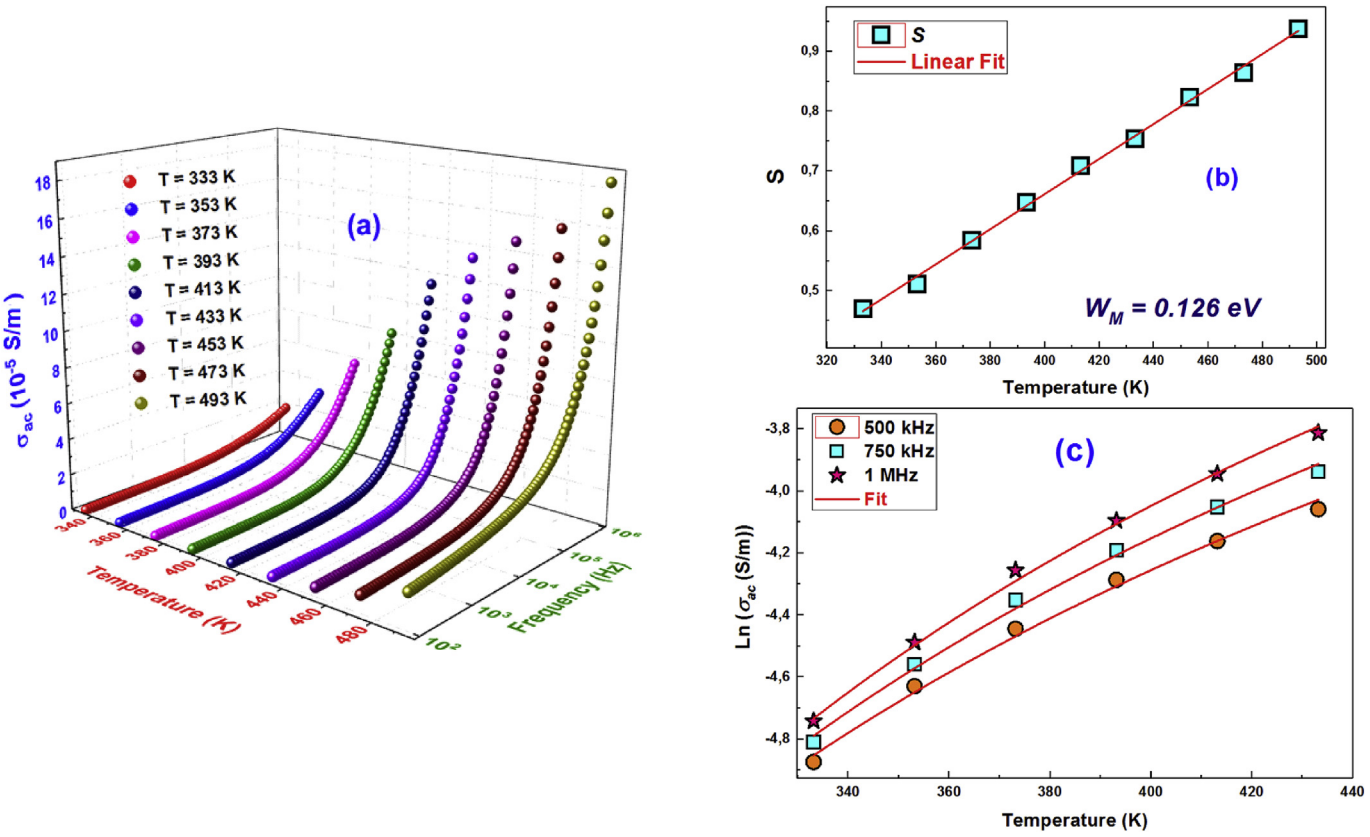

Fig. 12. **(a)** Frequency dependency of conductivity for BEBFCC compound, **(b)** Temperature dependence of the exponent S. **Inset**: the binding energy W_m value, **(c)** Temperature dependence of the NSPT model of conduction of the BEBFCC compound.

Table 4
The Jonscher's power-law fitting results of ac conductivity for BEBFCC compound.

Temperature	60	80	100	120	140	160	180	200
σ_{dc} (10^{-7} Sm^{-1})	3.732	6.451	9.214	1.990	12.443	27.250	65.131	120.9
A (10^{-10})	114.15	61.280	24.287	13.840	7.667	5.471	2.455	2.572
S	0.469	0.551	0.630	0.676	0.758	0.843	0.884	0.907

The Correlated **B**arrier **H**opping (CBH) model, the exponent "S" decreases with the increase in temperature [63].
The **O**verlapping **L**arge-**P**olaron **T**unneling (OLPT) model, the exponent S depends on both temperature and frequency and drops with increasing temperature to a minimum value and then rises when the temperature increases [64].
The **N**on-overlapping **S**mall **P**olaron **T**unneling (NSPT) model, the exponent "S" is temperature dependent. It increases with the increase of temperature [61].

As seen in Fig. 12 (b), the parameter S increase with the increase in temperature. Therefore, we can deduce that the NSPT model is the most suitable model to characterize the electrical conduction mechanism in the BEBFCC compound. According to this model, the exponent S could be calculated using the following expression [56]:

$$S = 1 + \frac{4k_BT}{W_m - k_BT\ln(\omega\tau_0)} \tag{6}$$

where Wm is the binding energy of the carrier in its localized sites and k_B the Boltzmann's constant. For the large values of W_m/k_BT, the parameter S becomes:

$$S = 1 + \frac{4k_BT}{W_m} \tag{7}$$

Based on Eq. (7) a linear fit of S (T) plot (red line in Fig. 12 (b)), the value of W_m was found around 0.126 eV.

Furthermore, according to the NSPT model the ac conductivity can be described by the following equation [61]:

$$\sigma_{ac} = \frac{(\pi e)^2 k_BT\alpha^{-1}\omega[N(EF)]^2R_\omega^4}{12} \tag{8}$$

where

$$R_\omega = \frac{1}{2\alpha}\left(\ln(1/\omega\tau_0) - \frac{W_H}{k_BT}\right) \tag{9}$$

α^{-1} is the spatial extension of polaron, N (E_F) is the density of states near the Fermi level, W_H is the polaron hopping energy and R_ω is the tunneling distance. The values N (E_F), α and W_H were adjusted to fit the calculated curves of ln (σ_{ac}) versus T to the experimental curves. The calculated fitting parameters using Eq. (8) and Eq. (9) are summarized in Table 5 and shown in Fig. 12 (c).

Table 5
Parameters used to NSPT model fitting for **BEBFCC** compound.

Frequency (kHz)	N_F ($x10^{39}$ $eV^{-1}m^{-1}$)	α ($Å^{-1}$)	R_ω (Å)	W_H (eV)
500	9.835	1.211	1.565	0.086
750	3.994	1.625	3.168	0.078
1000	1.428	0.711	3.763	0.077

The values of $N(E_F)$ were found to be reasonably high ($>10^{39}$ $eV^{-1}m^{-1}$), which suggests that the hopping between the pairs of sites dominates the mechanism of charge transport in the BEBFCC compound. Also, one can see that the values of the polaron hopping energy (W_H) are low even with increasing frequency which suggests that the hopping of polarons in this compound requires low energy aiding the jump from one site to another.

4. Conclusions

In summary, the $Bi_{0.8}Er_{0.1}Ba_{0.1}Fe_{0.96}Cr_{0.02}Co_{0.02}O_3$ (**BEBFCC**) multiferroic powder has been successfully prepared by the Sol-Gel method with the citric acid route. The nanoscale of the particles was confirmed by both DRX ($D_{SC} = 68$ nm) and SEM (88 nm) analysis. XRF and EDX analysis proved the presence of all integrated element during the synthesis. Comparing to the pure $BiFeO_3$, it's noticed that there is a slight change in intensity and the width of some Raman modes ($A_{1\text{-}3}$, $A_{1\text{-}1}$, $A_{1\text{-}2}$…) as a result of a variation of Fe–O and Bi–O bonds due to the substitution.

It was found that the dielectric relaxation and the conduction mechanism are strongly temperature dependent. Above 476 K, the activation energy deduced from the imaginary parts of both impedance (Z″) and Modulus (M″) and the ac conductivity was found to be around 1.4 eV. While, below this temperature the activation energy was found around 0.47 eV.

The presence of two contributions (grain and boundary grain) that contribute to the relaxation mechanism was confirmed by analyzing the Nyquist plots. It was found that both contributions have a close activation energies around 0.5 eV which confirms the presence of p-type polaron hopping conduction mechanism. According to the Jonscher's "S" parameter the Non-overlapping Small Polaron Tunneling hopping mechanism was confirmed for the BEBFCC compound.

Acknowledgments

The authors would like to acknowledge the financial support from FCT, Portugal (FCT/MCTES/BPD/42/25492/2016) and FEDER (POCI-01-0145-FEDER-007688).

Also, an acknowledgment goes to the support from the FEDER and from FCT (Project No. UID/FIS/04564/2016) and to the QREN-Mais Centro Project (No. ICT-2009-02-012-1890).

References

[1] E. Ascher, H. Rieder, H. Schmid, H. Stössel, Some Properties of ferromagnetoelectric nickel-iodine boracite, $Ni_3B_7O_{13}I$, J. Appl. Phys. 37 (1966) 1404–1405.
[2] T. Kimura, T. Goto, H. Shintani, K. Ishizaka, T. Arima, Y. Tokura, Magnetic control of ferroelectric polarization, Nature 426 (2003) 55–58.
[3] J. Wang, J.B. Neaton, H. Zheng, V. Nagarajan, S.B. Ogale, B. Liu, D. Viehland, V. Vaithyanathan, D.G. Schlom, U.V. Waghmare, N.A. Spaldin, K.M. Rabe, M. Wuttig, R. Ramesh, Epitaxial $BiFeO_3$ multiferroic thin film heterostructures, Science 299 (2003) 1719–1722.
[4] D.A. Sanchez, A. Kumar, N. Ortega, R.S. Katiyar, J.F. Scott, Near-room temperature relaxor multiferroic, Appl. Phys. Lett. 97 (2010), 202910.
[5] N.A. Hill, Why are there so few magnetic ferroelectrics? J. Phys. Chem. B 104 (2000) 6694–6709.
[6] I. Levin, M.G. Tucker, H. Wu, V. Provenzano, C.L. Dennis, S. Karimi, T. Comyn, T. Stevenson, R.I. Smith, I.M. Reaney, Displacive phase transitions and magnetic structures in Nd-substituted $BiFeO_3$, Chem. Mater. 23 (2011) 2166–2175.
[7] A.J. Mundy, M.C. Brooks, E.M. Holtz, A.J. Moyer, H. Das, F.A. Rébola, J.T. Heron, J.D. Clarkson, S.M. Disseler, Z. Liu, A. Farhan, R. Held, R. Hovden, E. Padgett, Q. Mao, H. Paik, R. Misra, L.F. Kourkoutis, E. Arenholz, A. Scholl, J.A. Borchers, W.D. Ratcliff, R. Ramesh, C.J. Fennie, P. Schiffer, D.A. Muller, D.G. Schlom, Atomically engineered ferroic layers yield a room-temperature magnetoelectric multiferroic, Nature 537 (2016) 523–527.
[8] W. Eerenstein, N.D. Mathur, J.F. Scott, Multiferroic and magnetoelectric materials, Nature 442 (2006) 759–765.
[9] T. Zhao, A. Scholl, F. Zavaliche, K. Lee, M. Barry, A. Doran, M.P. Cruz, Y.H. Chu, C. Ederer, N.A. Spaldin, R.R. Das, D.M. Kim, S.H. Baek, C.B. Eom, R. Ramesh, Electrical control of antiferromagnetic domains in multiferroic $BiFeO_3$ films at room temperature, Nat. Mater. 5 (2006) 823.
[10] G.W. Pabst, L.W. Martin, Y.H. Chu, R. Ramesh, Leakage mechanisms in $BiFeO_3$ thin films, Appl. Phys. Lett. 90 (2007), 072902.
[11] F. Yan, M.O. Lai, L. Lu, T.J. Zhu, Enhanced multiferroic properties and valence effect of Ru-doped $BiFeO_3$ thin films, J. Phys. Chem. C 114 (2010) 6994.
[12] P. Kharel, S. Talebi, B. Ramachandran, A. Dixit, V.M. Naik, M.B. Sahana, C. Sudakar, R. Naik, M.S.R. Rao, G. Lawes, Structural, magnetic, and electrical studies on polycrystalline transition-metal-doped $BiFeO_3$ thin films, J. Phys. Condens. Matter 21 (2009), 036001.
[13] Q.R. Yao, J. Cai, H.Y. Zhou, G.H. Rao, Z.M. Wang, J.Q. Deng, Influence of La doping on structure and magnetic behaviors in BiFeO3, J. Alloys Compd. 633 (2015) 170–173.
[14] J.B. Li, G.H. Rao, Y. Xiao, J.K. Liang, J. Luo, G.Y. Liu, J.R. Chen, Structural evolution and physical properties of Bi1-xGdxFeO3 ceramics, Acta Mater. 58 (2010) 3701–3708.
[15] B. Yotburut, P. Thongbai, T. Yamwong, S. Maensiri, Synthesis and characterization of multiferroic Sm-doped $BiFeO_3$ nanopowders and their bulk dielectric properties, J. Magn. Magn. Mater. 437 (2017) 51–61.
[16] M. Kumar, K.L. Yadav, Magnetic field induced phase transition in multiferroic $BiFe_{1-x}Ti_xO_3$ ceramics prepared by rapid liquid phase sintering, Appl. Phys. Lett. 91 (2007), 112911.
[17] J. Chen, J.L. Wang, H.Y. Dai, T. Li, Z.P. Chen, Investigations on the structure, defects, electrical and magnetic properties of Ni-substituted $BiFeO_3$ ceramics, J. Mater. Sci. Mater. Electron. 27 (2016) 11151–11157.
[18] J. Khajonrit, U. Wongpratat, P. Kidkhunthod, S. Pinitsoontorn, S. Maensiri, Effects of Co doping on magnetic and electrochemical properties of $BiFeO_3$ nanoparticles, J. Magn. Magn. Mater. 449 (2018) 423–434.
[19] J. Qi, Y.L. Zhang, Y.H. Wang, Y.Q. Liu, M.B. Wei, J.K. Zhang, M. Feng, J.H. Yang, Effect of Cr doping on the phase structure, surface appearance and magnetic property of $BiFeO_3$ thin films prepared via sol-gel technology, J. Mater. Sci. Mater. Electron. 28 (2017) 17490–17498.
[20] W.Y. Xing, Y.N.N. Ma, Y.L. Bai, S.F. Zhao, Enhanced ferromagnetism of Er-doped $BiFeO_3$ thin films derived from rhombohedral-to-orthorhombic phase transformations, Mater. Lett. 161 (2015) 216–219.
[21] H.W. Chang, F.T. Yuan, K.T. Tu, S.Y. Lin, C.R. Wang, C.S. Tu, Multiferroic properties of $Bi_{1-x}A_xFeO_3$ polycrystalline films on glass substrates (A = Ca, Sr, Ba and x=0.05-0.15), J. Alloys Compd. 683 (2016) 427–432.
[22] Y.J. Zheng, G.I. Tan, A. Xia, H.J. Ren, Structure and multiferroic properties of multi-doped $Bi_{1-x}Er_xFe_{0.96}Mn_{0.02}Co_{0.02}O_3$ thin films, J. Alloys Compd. 684 (2016) 438–444.
[23] L. Peng, H.M. Deng, J.J. Tian, Q. Rena, C. Penga, Z. Huanga, P.X. Yanga, J.H. Chua, Influence of Co doping on structural, optical and magnetic properties of $BiFeO_3$ films deposited on quartz substrates by sol–gel method, Appl. Surf. Sci. 268 (2013) 146–150.
[24] M.P.F. Graça, P.R. Prezas, M.M. Costa, M.A. Valente, Structural and dielectric characterization of LiNbO3 nano-size powders obtained by Pechini method, J. Sol Gel Sci. Technol. 64 (2012) 78–85.
[25] A. Benali, S. Azizi, M. Bejar, E. Dhahri, M.F.P. Graça, Structural, electrical and ethanol sensing properties of double-doping $LaFeO_3$ perovskite oxides, Ceram. Int. 40 (2014) 14367–14373.
[26] R.A. Young, The Rietveld Method, Oxford University Press, New York, 1993.
[27] A. Benali, M. Bejar, E. Dhahri, M. Sajieddine, M.P.F. Graça, M.A. Valente, Magnetic, Raman and Mössbauer properties of double-doping $LaFeO_3$ perovskite oxides, J. Mater. Chem. Phys. 149–150 (2015) 467–472.
[28] M.M. Costa, G.F.M. Pires Junior, A.S.B. Sombra, Dielectric and impedance properties' studies of the of lead doped (PbO)-Co_2Y type hexaferrite ($Ba_2Co_2Fe_{12}O_{22}$ (Co_2Y)), Mater. Chem. Phys. 123 (2010) 35.
[29] M. Muneeswaran, P. Jegatheesan, M. Gopiraman, I.S. Kim, N.V. Giridharan, Structural, optical, and multiferroic properties of single phased $BiFeO_3$, Appl. Phys. A 114 (2014) 853.
[30] M.S. Bernardo, T. Jardiel, M. Peiteado, F.J. Mompean, M. Garcia-Hernandez, M.A. Garcia, M. Villegas, A.C. Caballero, Intrinsic compositional inhomogeneities in bulk Ti-doped $BiFeO_3$: microstructure development and multiferroic properties, Chem. Mater. 25 (2013) 1533.
[31] J.G. Fisher, S.H. Jang, M.S. Park, H. Sun, S.H. Moon, J.S. Lee, A. Hussain, The Effect of niobium doping on the electrical properties of $0.4(Bi_{0.5}K_{0.5})TiO_3$-$0.6BiFeO_3$ lead-free piezoelectric ceramics, Materials 8 (2015) 8183–8194.
[32] N.V. Dang, T.D. Thanh, L.V. Hong, V.D. Lam, T.L. Phan, Structural, optical and magnetic properties of polycrystalline BaTi1-xFexO3 ceramics, J. Appl. Phys. 110 (2011), 043914.
[33] S.K. Pradhan, B.K. Roul, Effect of Gd doping on structural, electrical and magnetic properties of BiFeO3 electroceramic, J. Phys. Chem. Solids 72 (2011)

1180–1187.
[34] A. Guinier, in: X. Dunod (Ed.), Théorie et Technique de la radiocristallographie, third ed., 1964, p. 462.
[35] E.V. Ramana, A. Mahajan, M.P.F. Graca, A. Srinivas, M.A. Valente, Ferroelectric and magnetic properties of magnetoelectric $(Na_{0.5}Bi_{0.5})TiO_3$-$BiFeO_3$ synthesized by acetic acid assisted sol-gel method, J. Eur. Ceram. Soc. 34 (2014) 4201–4211.
[36] M.K. Singh, H.M. Jang, S. Ryu, M.-H. Jo, Polarized Raman scattering of multiferroic $BiFeO_3$ epitaxial films with rhombohedral R3c symmetry, Appl. Phys. Lett. 88 (2006), 042907.
[37] R. Haumont, J. Kreisel, P. Bouvier, F. Hippert, Phonon anomalies and the ferroelectric phase transition in multiferroic $BiFeO_3$, Phys. Rev. B 73 (2006), 132101.
[38] P. Hermet, M. Goffinet, J. Kreisel, P. Ghosez, Raman and infrared spectra of multiferroic bismuth ferrite from first principles, Phys. Rev. B 75 (2007), 220102.
[39] P.C. Sati, M. Kumar, S. Chhoker, M. Jewariya, Influence of Eu substitution on structural, magnetic, optical and dielectric properties of $BiFeO_3$ multiferroic ceramics, Ceram. Int. 41 (2015) 2389–2398.
[40] L.Y. Chang, C.S. Tu, P.Y. Chen, C.S. Chen, V.H. Schmidt, H.H. Wei, D.J. Huang, T.S. Chan, Raman vibrations and photovoltaic conversion in rare earth doped $(Bi_{0.93}RE_{0.07})FeO_3$ (RE = Dy, Gd, Eu, Sm) ceramics, Ceram. Int. 42 (2016) 834–842.
[41] F. Borsa, D.R. Torgeson, S.W. Martin, H.K. Patel, Relaxation and fluctuations in glassy fast-ion conductors: wide-frequency-range NMR and conductivity measurements, Phys. Rev. B 46 (1992) 795.
[42] F.S.H. Abu-Samaha, M.I.M. Ismail, AC conductivity of nanoparticles $Co_xFe_{(1-x)}Fe_2O_4$ (x = 0, 0.25 and 1) ferrites, Mater. Sci. Semicond. Process. 19 (2014) 50–56.
[43] E. Venkata Ramana, S.V. Suryana Rayana, T. Bhima Sankaram, ac impedance studies on ferroelectromagnetic $SrBi_{5-x}La_xTi_4FeO_{18}$ ceramics, Mater. Res. Bull. 41 (2006) 1077.
[44] N. Chihaoui, R. Dhahri, M. Bejar, E. Dharhi, L.C. Costa, M.P.F. Graça, Electrical and dielectric properties of the $Ca_2MnO_{4-\delta}$ system, Solid State Commun. 151 (2011) 1331–1335.
[45] P. Tirupathi, A. Chandra, Grain and grain boundary effects in Ca^{2+} doped $BiFeO_3$ multiferroic ceramics, Phys. Status Solidi B 249 (2012) 1639–1645.
[46] Chen Ang, Zhi Yu, L.E. Cross, Oxygen-vacancy-related low-frequency dielectric relaxation and electrical conduction in Bi:$SrTiO_3$, Phys. Rev. B 62 (2000) 228–236.
[47] H. Rahmouni, A. Benali, B. Cherif, E. Dhahri, M. Boukhobza, K. Khirouni, M. Sajieddine, Structural and electrical properties of $Zn_{1-x}Ni_xFe_2O_4$ ferrite, Phys. B Condens. Matter 466–467 (2015) 31–37.
[48] E. Barsoukov, J. Ross Macdonald, Impedance Spectroscopy Theory, Experiment and Applications, second ed., Wiley Interscience, New York, 2005, p. 14.
[49] U. Intatha, S. Eitssayeam, J. Wang, T. Tunkasiri, Impedance study of giant dielectric permittivity in $BaFe_{0.5}Nb_{0.5}O_3$ perovskite ceramic, Curr. Appl. Phys. 10 (2010) 21.
[50] A. Omri, M. Bejar, E. Dhahri, M. Es-Souni, M.A. Valente, M.P.F. Graça, L.C. Costa, Electrical conductivity and dielectric analysis of $La_{0.75}(Ca,Sr)_{0.25}Mn_{0.85}Ga_{0.15}O_3$ perovskite compound, J. Alloys Compd. 536 (2012) 173–178.
[51] O. Bohnke, J. Emery, J.L. Fourquet, Anomalies in Li^+ ion dynamics observed by impedance spectroscopy and 7Li NMR in the perovskite fast ion conductor $(Li_{3x}La_{2/3-x\ 1/3-2x})TiO_3$, Solid State Ionics 158 (2003) 119.
[52] N. Elghoul, M. Wali, S. Kraiema, H. Rahmouni, E. Dhahri, K. Khirouni, Sodium deficiency effect on the transport properties of $La_{0.8}Na_{0.2-x}\square_xMnO_3$ manganites, Physica B 478 (2015) 108–112.
[53] J. Yang, B.C. Zhao, Y.Q. Ma, R.L. Zhang, R. Ang, W.H. Song, Y.P. Sun, Small-polaron hopping conduction in $La_{0.9}Te_{0.1}MnO_3$ above the metal-insulator transition, Mater. Lett. 60 (2006) 3281.
[54] N. Masó, A.R. West, Electrical properties of Ca-doped BiFeO3 ceramics: from p-type semiconduction to oxide-ion conduction, Chem. Mater. 24 (2012) 2127–2132.
[55] M.P.F. Graça, M.G.F. da Silva, A.S.B. Sombra, M.A. Valente, The dielectric behavior of a thermoelectric treated B_2O_3–Li_2O–Nb_2O_5 glass, J. Non Cryst. Solids 354 (2016) 3408–3413.
[56] M.P.F. Graça, M.G.F. da Silva, A.S.B. Sombra, M.A. Valente, Electrical characterization of SiO_2: $LiNbO_3$ glass and glass–ceramics using dc conductivity, TSDC measure-ments and dielectric spectroscopy, J. Non Cryst. Solids 353 (2007) 4390–4394.
[57] E. Barsoukov, J. Ross Macdonald, Impedance Spectroscopy Theory, Experiment and Applications, second ed., Wiley Interscience, New York, 2005, p. 14.
[58] S. Lanfredi, P.S. Saia, R. Lebullenger, A.C. Hernandes, Electric conductivity and relaxation in fluoride, fluorophosphate and phosphate glasses: analysis by impedance spectroscopy, Solid State Ionics 146 (2002) 329.
[59] S.R. Elliot, Ac conduction in amorphous chalcogenide and pnictide semiconductors, Adv. Phys. 36 (1987) 135–217.
[60] M. Ben Bechir, K. Karoui, M. Tabellout, K. Guidara, A. Ben Rhaiem, Electric and dielectric studies of the $[N(CH_3)_3H]_2CuCl_4$ compound at low temperature, J. Alloys Compd. 588 (2014) 551–557.
[61] A. Ghosh, Frequency-dependent conductivity in bismuth-vanadate glassy semiconductors, Phys. Rev. B 41 (1990) 1479.
[62] M. Pollak, On the frequency dependence of conductivity in amorphous solids, Philos. Mag. 23 (1971) 519–542.
[63] S. Mollah, K.K. Som, K. Bose, B.K. Chaudhuri, Ac conductivity in $Bi_4Sr_3Ca_3Cu_yO_x$ (y=0–5) and $Bi_4Sr_3Ca_{3-z}Li_zCu_4O_x$ (z=0.1–1.0) semiconducting oxide glasses, J. Appl. Phys. 74 (1993) 931.
[64] M. Megdiche, C. Perrin–Pellegrino, M. Gargouri, Conduction mechanism study by overlapping large-polaron tunnelling model in SrNiP2O7 ceramic compound, J. Alloys Compd. 584 (2014) 209–215.